Elastoplastic Deformation in a Wedge-Shaped Plate Caused By a Subducting Seamount

Min Ding*[1], and Jian Lin[2]
[1]MIT/WHOI Joint Program, [2]Woods Hole Oceanographic Institution
*Woods Hole Oceanographic Institution, MS 22, Woods Hole, MA 02543, dingmin@mit.edu

Abstract: We used COMSOL Multiphysics 4.3 to simulate elastoplastic deformation and plastic strain in a wedge-shaped plate above a subduction zone caused by the movement of a subducting seamount. The modeling results revealed that a pair of conjugate normal faults would first appear in the thinner part of the plate. Subsequently, a second pair of conjugate thrust faults would form in the thicker part of the plate. The durations of the seamount movement required for these faults to cut through the entire plate are longer for deeper seamounts, greater dipping angles of the plate, and for the Mohr-Coulomb than the Von Mises criterion. Our models provide a quantitative way to investigate the time-dependent lithospheric deformation and fault formation processes during seamount subduction.

Keywords: Elastoplasticity, seamount subduction, fault-like shear zones

1. Introduction

The goal of this investigation is to test a conceptual hypothesis that a subducting seamount (Figure 1) might generate a complex fault system in the upper plate [*Wang and Bilek*, 2011]. The fault system and its stress state were envisioned to evolve with time due to the geometrical movement of the seamount.

We conducted a series of static numerical experiments using COMSOL Multiphysics 4.3 to investigate the evolution of the fault-like shear zones (thereafter referred to as faults) in the upper plate caused by the seamount subduction. The model parameter space explored includes seamount depth, D, plate dipping angle, θ, and plastic failure criteria, Von Mises and Mohr-Coulomb. In particular, we calculated the durations of seamount movement that are required for the failure zones to cut through the entire upper plate, assuming a steady-state seamount movement rate of 5 cm/yr. These through-going faults in the upper plate might be prone to moderate to large earthquakes.

These numerical models provide a quantitative way to investigate the time-dependent deformation of the upper plate during seamount subduction.

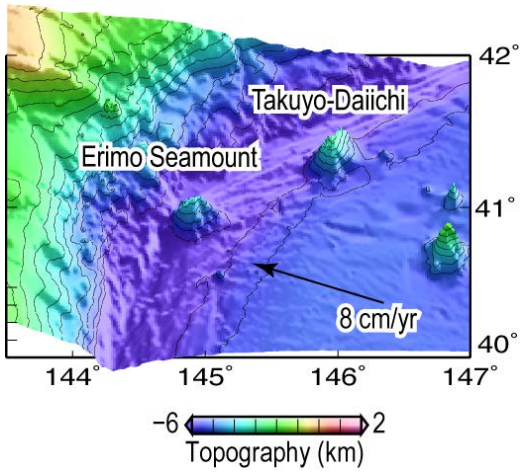

Figure 1. 3D perspective of surface topography of the flat-topped Erimo and conical Takuyo-Daiichi seamounts near the Japan Trench.

2. Use of COMSOL Multiphysics

2.1 Elastoplastic material

We modeled the mechanical failure using the Mohr-Coulomb failure law, which is a model for elastic perfectly-plastic material.

The shear strength of the material is given by

$$\tau = \tan(\phi)\sigma_n + C, \quad (1)$$

where ϕ is the angle of the internal friction, σ_n is the normal stress caused by the seamount subduction plus the background hydrostatic pressure ρgz, where ρ = 2.7 g/cm^3 is the density of the upper plate, g = 9.8 m/s^2 is the gravity acceleration. We assumed that the cohesion, $C = c\rho gz$, is depth dependent and c = 0.5 is the coefficient of the cohesion over the hydrostatic pressure (Figure 2$_a$). If ϕ = 0^o, the Mohr Coulomb failure criterion reduces to the Von Mises criterion.

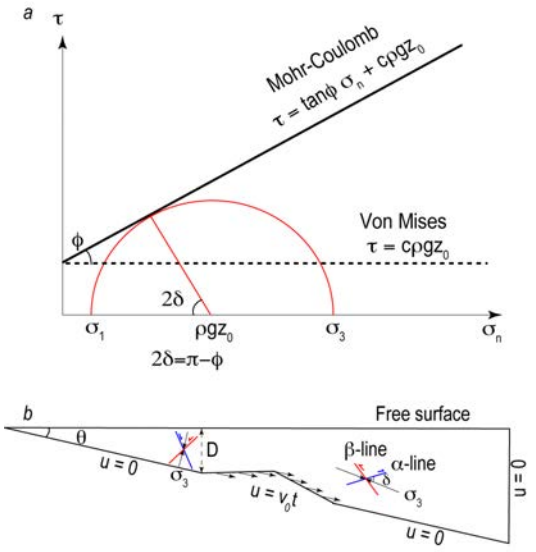

Figure 2. (a) Failure criterion used in our models. Mohr's circle (red) at a point of depth z_0. Compression stress is positive. σ_3 and σ_1 are the maximum and minimum compressional principal stresses, respectively. (b) Model set-up and anticipated stress field.

In COMSOL Multiphysics software, the Mohr-Coulomb strength is defined by the yield function, F:

$$F = \frac{\tan\phi}{\sqrt{9+12\tan^2\phi}}\sigma_{ii} + \sqrt{\frac{1}{2}s_{ij}s_{ij}}, \qquad (2)$$

where σ_{ij} is the stress tensor, s_{ij} is the deviatoric stress tensor, and $\sqrt{\frac{1}{2}s_{ij}s_{ij}}$ is the equivalent deviatoric stress. When F becomes equal to the cohesion, C, material begins to fail. F will stay equal to C for perfect-plastic deformation afterward.

The COMSOL system then determines the plastic strain tensor ε_{ij}^p by solving the equations of plastic flow law:

$$\frac{\delta\varepsilon_{ij}^p}{\delta t} = \lambda\frac{\partial F}{\partial\sigma_{ij}}, \qquad (3)$$

$$\varepsilon_{ij}^p = \int\frac{\delta\varepsilon_{ij}^p}{\delta t}\delta t, \qquad (4)$$

where $\frac{\delta}{\delta t}$ stands for differentiation with respect to pseudo-time, while plastic multiplier λ is determined by complementary conditions:

$$F \le C, \lambda \ge 0, (F-C)\lambda = 0. \qquad (5)$$

The elastic stress-strain relationship, i.e., the Hooke's law, and the decomposition of elastic and plastic strain are described by the following equations, respectively:

$$\sigma_{ij} = C_{ijkl}(\varepsilon_{kl} - \varepsilon_{kl}^p), \qquad (6)$$

$$C_{ijkl} = \lambda\delta_{ij}\delta_{kl} + \mu(\delta_{ik}\delta_{jl} + \delta_{il}\delta_{jk}), \qquad (7)$$

where C_{ijkl} is the stiffness tensor, $\varepsilon_{jk} - \varepsilon_{jk}^p$ is the elastic strain tensor, $\lambda = E\nu/(1+\nu)/(1-2\nu)$ and $\mu = E/2(1+\nu)$ are elastic moduli, and δ_{ij} is the Kronecker delta. We assume Poisson's ratio, ν = 0.25, and Young's modulus, $E = 8 \times 10^{10}$ Pa. The material is assumed to be in stress equilibrium:

$$\sigma_{ij,j} = 0, \sigma_{ij} = \sigma_{ji}. \qquad (8)$$

The yield criterion (Equation 1), Hooke's law for elastic behavior (Equation 6), flow law for plastic behavior (Equation 3), and the mechanical equilibrium equations (Equation 8) are solved under pre-described boundary conditions. The plastic strain tensor, ε_{ij}^p, total strain tensor, ε_{ij}, and stress tensor, σ_{ij}, are time-dependent variables to be solved.

2.2 Model set-up

The model domain represents a cross section of the upper plate with an upward-pointed triangular notch to represent the seamount (Figure 2b). The top surface of the model was assumed to be stress free, while the right side and the subduction interface were assigned fixed displacements. Due to the seamount movement, the section of the subduction interface between the seamount and the upper plate was subjected to a displacement vector parallel to the plate dipping direction, $u = v_0t$, where t is the time duration of seamount movement from the beginning of the process, and v_0 is the seamount movement velocity.

The conical shape of the seamount is analogous to the Takuyo-Daiichi seamount (Figure 1) [*Dominguez et al.*, 1998]. We also modeled a flat-topped seamount, similar to the Erimo seamount; the results were found to be similar to that for a conical seamount. Here we show results for a conical seamount with a base width of 30 km and height of 3 km. For plate dipping angles, θ = 0°, 10°, and 20°, we calculated both the Von Mises (ϕ = 0°) and Mohr-Coulomb (ϕ = 30°) failure. We defined a characteristic time $T_0 = 0.001\ D/v_0$, where D is the plate thickness at the left base of the

seamount (Figure 2b). Model parameters tested in this study are listed in Table 1.

Table 1: Model parameters

Parameter	Description	Value
ϕ	Angle of internal friction (^{o})	0, 30
θ	Dipping angle (^{o})	0, 10, 20
D	Distance from the left side of the seamount base to the ground surface (km)	5, 10, 20
v_0	Seamount subduction velocity (km/yr)	$5x10^{-5}$
T_0	0.001 D/v_0 (yr)	100, 200, 400

2.3 Numerical modeling

We adopted a triangular meshing scheme with a maximum grid size of 1 km and finer grids of 0.5 km surrounding the seamount (Figure 3).

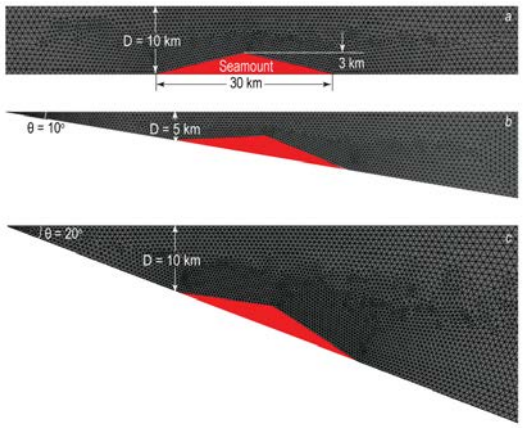

Figure 3. Meshes for modeling deformation in the upper plate with different plate dipping angle, θ = 0^o, 10^o, and 20^o.

The quasi-static deformation of the upper plate was calculated using a stationary solver with the seamount displacement, u, sweeping from zero to a value large enough for material to fail.

3. Modeling Results

The modeling results illustrate the formation of two distinctive groups of faults caused by the seamount movement. A pair of conjugate normal faults first appeared on the left side of the seamount in the thinner part of the plate. The right- and left-dipping normal faults were observed to cut though the entire plate at $t = T_1$ and T_2, respectively (Figures 4$_{a-b}$). Subsequently, a pair of thrust faults emerged on the right side of the seamount in the thicker part of the plate. The right- and left-dipping thrust faults were observed to cut through the plate at $t = T_3$ and T_4, respectively (Figures 4$_{c-d}$). For the specific parameters used in this study, the calculated durations for normal faults to cut through the entire plate, T_1 and T_2, are in the range of 200-3,000 yrs, while that for the through-cutting thrust faults, T_3 and T_4, are in the range of 200-16,000 yrs (Table 2).

Model results show that the required fault formation times, T_1 to T_4, are greater for the Mohr-Coulomb failure criterion than for the Von Mises material. The predicted dipping angles of the normal and thrust faults also depend on the failure criteria. The dipping angles of the normal faults, α_1 and α_2, are calculated to be 47°-58^o for the Von Mises and 58°-80^o for the Mohr-Coulomb criterion, respectively. The calculated dipping angles of thrust faults, α_3 and α_4, fall into the range of 47°-58^o for the Von Mises and 31°-45^o for the Mohr-Coulomb criterion, respectively.

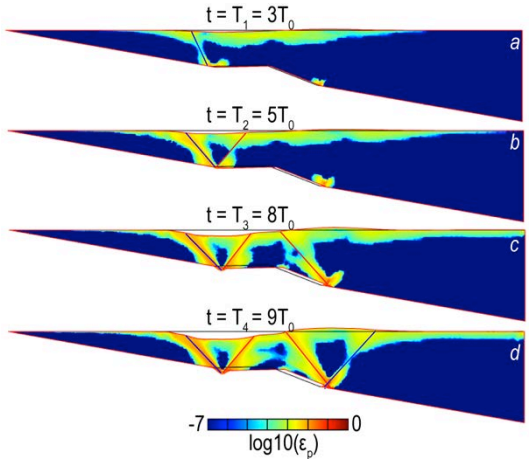

Figure 4. Snapshots showing a sequence of faults cutting though the entire plates (results of Model 2b): (a) right-dipping normal fault; (b) left-dipping normal fault; (c) right-dipping thrust fault; and (d) left-dipping thrust fault. ε_p is the second invariant of the plastic strain tensor, with dark blue color indicating elastic regions. Deformation of the model domain is exaggerated by a factor of 50.

3.1 Differences between elasticity and elastoplasticity

We illustrate slip lines in the upper plate for both elastic (Figure $5_{a\text{-}b}$) and elastoplastic (Figure $5_{c\text{-}d}$) models. The α- and β-slip lines represent right-lateral and left-lateral shear stress along the maximum shear stress planes, respectively. The slip lines lie at an angle of $\delta=(\pi-\phi)/2$ to the direction of maximum compression, σ_3. The slip lines indicate possible fault slip directions.

Slip lines for the elastic and elastoplastic materials are similar for internal friction angle, ϕ = 0° (Figures 5a and 5c) and ϕ = 30° (Figures 5b and 5d), respectively. However, the use of elastoplasticity enables us to predict plastic shear zones (gray-color regions in Figures 5c and 5d), where through-going faults might form.

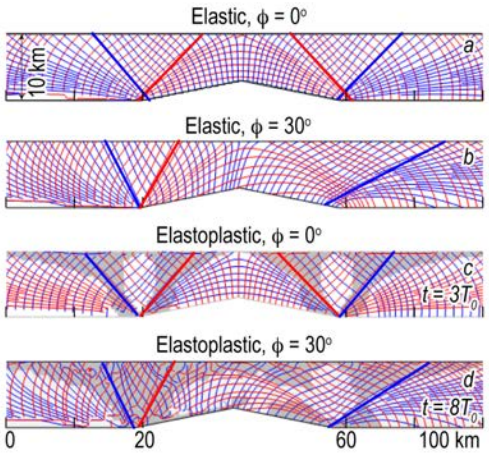

Figure 5. Calculated distribution of slip lines for elastic and elastoplastic rheology. (a) Elastic rheology with internal friction angle, ϕ = 0°. (b) Elastic and ϕ = 30°. (c) Elastoplastic rheology assuming Von Mises yield criteria, ϕ = 0°. Gray color indicates fault zones (results of Model 1a). (d) Elastoplastic rheology assuming Mohr-Coulomb failure with ϕ = 30° (results of Model 1b).

3.2 Differences between the Von Mises and Mohr-Coulomb failure

The differences in the shape of the shear zones calculated for the Von Mises and Mohr-Coulomb yield criteria are clearly visible in Figure 6. For the Von Mises material (θ = 0°, Model 1a), the pairs of normal and thrust faults formed at the same time (Figure 6a). For the Mohr-Coulomb material, however, the normal faults appeared prior to the formation of thrust faults (Figures 6b and 6c).

The dipping angles of the normal faults, α_1 and α_2, were calculated to be 47°-58° for the Von Mises criterion and 58°-80° for the Mohr-Coulomb criterion, respectively (Figure 6a, Table 2). For the thrust faults, α_3 and α_4 were calculated to be in the range of 47°-58° for the Von Mises criterion and 31°-45° for the Mohr-Coulomb criterion, respectively (Figure 6b,c, Table 2). These calculated shear zone dipping angles are consistent with the prediction of the slip line theory (Figure 5).

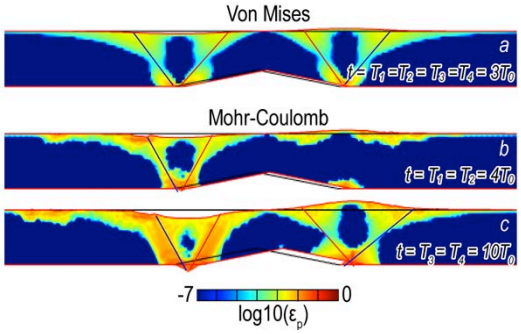

Figure 6. Snapshots showing the formation of through-going faults in the upper plate above a flat subduction interface (i.e., plate dipping angle is zero). (a) For Von Mises material (results of Model 1a). (b) For Mohr-Coulomb material when normal faults (left of the seamount) cut through the entire plate (results of Model 1b). (c) For Mohr-Coulomb material when thrust faults (right of the seamount) also cut through the entire plate (results of Model 1b).

3.3 Influence of the seamount depth and dipping angle

With increasing seamount depth, D, longer durations of seamount movement, T_1 to T_4, are required for the faults to cut through the upper plate (Figure 7, Table 2).

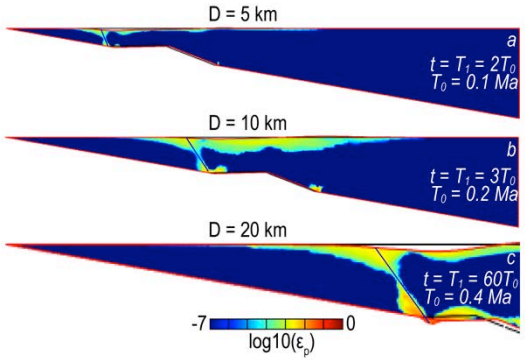

Figure 7. Snapshots showing the right-dipping normal fault cutting through the entire plate. (a) For seamount depth, D = 5 km (results of Model 2a). (b) D = 10 km (results of Model 2b). (c) D = 20 km (results of Model 2c).

The plate dipping angle, θ, has a similar effect as the seamount depth, D. Longer durations of seamount movement are required for faults to cut through plates of greater dipping angles (Figure 8, Table 2).

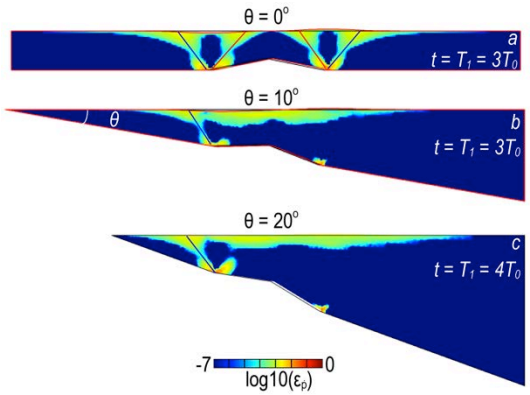

Figure 8. Snapshots showing the right-dipping normal fault cutting through the entire plate. (a) Plate dipping angle, $\theta = 0^o$ (results of Model 1a). (b) $\theta = 10^o$ (results of Model 2b). (c) $\theta = 20^o$ (results of Model 4b).

4. Conclusions

Our modeling results illustrate the formation of fault-like shear zones in the upper plate of a subduction system caused by seamount movement. Modeling results predicted a region of extension on the thinner part of the plate, where a pair of conjugate normal faults first formed and eventually cut through the entire plate. Meanwhile, a region of compression appeared on the thicker part of the plate, where a pair of conjugate thrust faults later formed. The durations of the seamount movement required for these faults to cut through the entire plate are longer for deeper seamounts, greater dipping angles of the plate, and for the Mohr-Coulomb than for the Von Mises criterion.

Our models provide a quantitative way to analyze the fault system evolution caused by subducting seamount for different subduction zone geometry and upper plate material properties.

5. References

1. Dominguez, S., S. Lallemand, J. Malavieille, and R. von Huene, Upper plate deformation associated with seamount subduction, *Tectonophysics*, **293**, 207-224 (1998)
2. Wang, K., and S. L. Bilek, Do subducting seamounts generate or stop large earthquakes?, *Geology*, **39**, 819-822 (2011)

6. Acknowledgements

Our study benefitted from discussion with Mark Behn, Jean-Arthur Olive, Hongfeng Yang, Jeff McGuire, and Brian Tucholke of the Woods Hole Oceanographic Institution, as well as Charles Williams of the GNS Science Institution. We thank COMSOL Help Group and Srikanth Vaidianathan at the COMSOL Inc. for technical support.

Table 2: Modeling results

Model number	Input				Output							
	θ(°)	ϕ(°)	D(km)	T_0(yr)	T_1/T_0	α_1(°)	T_2/T_0	α_2(°)	T_3/T_0	α_3(°)	T_4/T_0	α_4(°)
1a	0	0	10	200	1	51	1	49	1	58	1	48
1b	0	30	10	200	4	58	4	55	10	45	10	41
2a	10	0	5	100	1.5	52	2	49	5.5	48	8	47
2b	10	0	10	200	2.5	49	4.5	54	7	49	9	48
2c	10	0	20	400	6	58	N/A	N/A	N/A	N/A	20.5	57
3a	10	30	5	100	2	63	2	52	18	39	18	31
3b	10	30	10	200	5	63	5	61	N/A	N/A	21	34
3c	10	30	20	400	8	60	13	63	N/A	N/A	22	45
4a	20	0	5	100	2	50	2	50	13	47	13	48
4b	20	0	10	200	4	49	4	52	N/A	N/A	12.5	50
4c	20	0	20	400	7.5	49	N/A	N/A	N/A	N/A	18	51
5a	20	30	5	100	3	63	9	50	N/A	N/A	52	38
5b	20	30	10	200	5	79	7	43	N/A	N/A	49	35
5c	20	30	20	400	7.5	80	N/A	N/A	N/A	N/A	40	41

T_0: Characteristic time defined as $T_0 = 0.001\ D/v_0$. In this study, v_0 is fixed to be $5\text{x}10^{-5}$ km/yr.
T_1 to T_4: Time durations of seamount movement required for a sequence of faults to cut through the upper plate, respectively. T_1 is for the right-dipping normal fault, T_2 for the left-dipping normal fault, T_3 for the right-dipping thrust fault; and T_4 for the left-dipping thrust fault (Figure 4). N/A refers to the cases when a specific fault branch was not distinguishable in the model results.
α_1 to α_4: Dipping angles of the through-going faults.